CFD Letters

Journal homepage:
https://semarakilmu.com.my/journals/index.php/CFD_Letters/index
ISSN: 2180-1363

Numerical Model Parameters Choice of Helical Savonius Wind Rotor: CFD Investigation and Experimental Validation

Mariem Lajnef[1,*], Mabrouk Mosbahi[2,3], Hasna Abid[1], Zied Driss[1], Emanuele Amato[3,4], Tullio Tucciarelli[3,4], Marco Sinagra[4]

[1] Laboratory of Electro-Mechanic Systems (LASEM), National School of Engineers of Sfax (ENIS), University of Sfax, B.P. 1173, km 3.5 Soukra, 3038 Sfax, Tunisia
[2] University of Tunis, Higher National Engineering School of Tunis (ENSIT), Avenue Taha Hussein Montfleury, 1008 Tunisia
[3] University of Palermo, Department of Engineering, 90128, Italy
[4] Sustainable Mobility center (Centro Nazionale per la Mobilita Sostenible-CNMS), Italy

ARTICLE INFO

Article history:
Received 11 October 2023
Received in revised form 12 November 2023
Accepted 15 December 2023
Available online 31 May 2024

Keywords:
Helical Savonius wind rotor; wind tunnel; numerical model; power coefficient; torque coefficient

ABSTRACT

Electrical power is essential for human beings welfare. The available wind as a clean and renewable source of energy has whetted extensive interest over decades. Savonius vertical axis wind rotor as an energy converter has the merit of being adequate for specific implementations owing to its lower cost and independency on wind direction. From this perspective, multiple studies have been conducted to boost its efficiency. This research work emphasizes on the helical Savonius wind rotor (HSWR). The basic objective is to investigate the impact of selecting the numerical model parameters on its aerodynamic and performance characteristics. Experimental tests were realized with a 3D printed HSWR in a wind tunnel. The experimental performances in terms of power, static and dynamic torque coefficients were addressed. Next, a numerical study was undertaken through Ansys Fluent 17.0 software. Grid, turbulence model and rotating domain size tests were examined. Good accordance was obtained, which validated the numerical model with an averaged error of 5%. The maximum power coefficient proved to be equal to 0.124 at a tip speed ratio of 0.73 and 0.1224 at a tip speed ratio of 0.69, respectively, numerically and experimentally.

1.Introduction

Currently, electrical energy has become an indicator of modern civilization. Fossil fuels presides energy sources used to generate electricity all over the world. Owing to its excessive use, the world has started suffering from its depletion with the emergence of several environmental problems. As a green, environmental friendly and renewable source of energy, the wind energy has been invested as an alternative to fossil fuels [1-3]. Wind turbines are identified as wind energy converters and multiple designs have been elaborated over decades.

* *Corresponding author.*
E-mail address: mariem.lajnef@enis.tn (Mariem Lajnef)

https://doi.org/10.37934/cfdl.16.10.94111

Known for their low cost of installation and maintenance, their independency on wind direction, vertical axis wind turbines (VAWT) proved to be adequate for specific implementations. Among the VAWT, Savonius turbines display numerous merits: having the cheapest as well as the simplest design with a significant self-starting torque and independence to wind direction. However, its efficiency remains poor. Relying upon the literature review, the classical Savonius wind turbine has drown extensive interest. Indeed, researchers have conducted much researches to improve its efficiency through the optimization of its geometrical parameters. The amount of studies looking at computational approaches has expanded recently. With this regard, Akwa *et al.,* [4] investigated the overlap ratio defined by the ratio between the overlap distance and the blade chord with the intention of the Savonius rotor performance betterment. They studied numerically the effect of five overlap ratios ranging from 0 to 0.6. They found an optimum value of 0.15 which corresponds to a maximum power coefficient of 0.316 at a tip speed ratio of 1.25. Roy *et al.,* [5] studied six overlap ratios varying from 0 to 0.3 on a single stage Savonius wind turbine to investigate the overlap ratio effect on the static torque. With an overlap ratio higher than 0.2, the static torque decreased for the tested velocities. Zhao *et al.,* [6] depicted the effect of the aspect ratio on a two bladed helical Savonius rotor. They putted to test numerically five aspect ratios varying from 1 to 7. They found that the rotor having an aspect ratio equal to 6 was the optimum one with an improved power coefficient of 0.21 but with a reduced rotating speed. Jeon *et al.,* [7] investigated numerically the effect of the end plates addition on the torque and the power coefficients of a 180° twisted Savonius rotor. The studied rotors were taken, respectively, without end plates, with only lower end plate and with both upper and lower end plates. To show the effect of the end plate size and shape, they varied the ratio between the end plate area to the cross sectional area. The end plates size affected the maximum output power coefficient which increased with the rise of end plate size. Thus, the upper and lower end plates with circular shape were found the optimum design that improved the efficiency of the studied helical Savonius rotor by 36% at a wind velocity of 10 $m.s^{-1}$ over the non-end plates design. Zheng *et al.,* [8] carried out a numerical study for modified Savonius rotor with four, five and six blades. They found that the maximum power coefficient was equal to 27.14%, 28.493% and 30.564% at a rotating speed equal to 17.206, 16.265 and 18.369 rpm, respectively for four, five and six bladed rotors. The efficiency of the modified Savonius rotor increases with the increase of the blades number. Thus, the six-bladed design was found the optimum. Kothe *et al.,* [9] treated a helical Savonius rotor with 180° twist angle. They numerically compared it to a two-stage conventional one keeping the same parameters. The helical rotor processed more with higher power coefficient and more stable torque and with less variation. Lee *et al.,* [10] investigated the performance of a two bladed helical Savonius rotor at different twist angles of 0°, 45°, 90° and 135° ,respectively, under the same aspect ratio and projected area. The power coefficient and the torque coefficient were evaluated both numerically at different tip speed ratios. With regard to the power coefficient, it occurred its maximum value of 0.13 at a twist angle of 45°. However, for the 90° and 135° twist angles, the power coefficient was lower even than 0°. For the torque coefficient, the maximum values of 90° and 135° were less important than 0° and 45°. In fact, beyond 90° the torque coefficient became more stabilized and constant in terms of its variation for different azimuth angles. Under the same conditions, some prominent blade shapes of Savonius wind rotor have been studied by Alom *et al.,* [11] to evaluate their performances. The tested rotors have, respectively, semi-circular, Benech, modified-Bach and elliptical blade shapes. According to the two-dimensional unsteady simulations, the elliptical shape provided the highest maximum power coefficient of 0.34 over the modified Bach (0.304), the Benech (0.294) and the semi-circular (0.272) at a tip speed ratio of 0.8. Tian *et al.,* [12] introduced the optimization of the Savonius rotor by acting on the ellipcity of both concave and convex side of the rotor blade. With a suitable sizing study, they found an optimal design

that gave a maximum power coefficient of 0.258 which is 4.41% higher than the conventional design. In the same context, a CFD investigation was carried out by Syahreen *et al.,* [13] to assess the performance of a Savonius wind turbine with a novel blade shape design. The wind speed impact was studied. An improvement of 20 % was recorded with the novel design over the classical elliptical Savonius wind rotor. Besides, a new model of Savonius wind turbine was numerically examined by Sohib *et al.,* [14] through the addition of tubercles at the level of the rotor blades. With an improvement of up to 46.15 %, the new turbine model fitted with tubercles outperformed the baseline model. The flow visualizations revealed decreased wake diameters, which indicate less drag and ultimately results in a better performance when compared to the baseline model. Mohamed *et al.,* [15] shielded a portion of the returning blade of a Savonius wind rotor with both two and three blades using a deflecting plate through the use of CFD simulations. They discovered that it enhanced the capacity for self-starting resulting in a positive static moment for all angular locations. For the two and three-bladed rotors, respectively, the shielding obstacle gave an increase in the maximum power coefficient of 27.3% and 27.5%. The addition of an air deflector made of a pair of curtains placed in front of a two-bladed Savonius wind rotor was investigated numerically by Maldonado *et al.,* [16]. They discovered that it enhanced the incoming velocity by up to 32% subsequently the rotor outputs were improved.

A scrutiny of researches addressing the HSWR finds a dearth of studies that handle their optimization. In view of the complex geometry of its blades, the HSWR has not been thoroughly deciphered and the majority of investigations were restricted to the conventional form. As previously stated, computational methods were employed to analyze the performance of Savonius wind rotor. The selection of the numerical model parameters is a delicate and necessary task to be relevant. As far as our work is concerned, the basic objectives are to assess the performance of a HSWR and to investigate the numerical model parameters effect on it namely the grid sensitivity, the turbulence model and the rotating domain size. Experimental tests were undertaken on a 3D printed HSWR putted in a wind tunnel. A numerical study was realized through 3D transient simulations investing the CFD Ansys Fluent 17.0 software.

2. Experimental method

2.1 Turbine Layout and Fabrication

Referring the geometrical complexity of the HSWR, 3D printing technology was used as a manufacturing process. Initially, the tested rotor was designed using Solidworks software (Figure 1(a)). Afterwards, the digital model was fed into a 3D printer, which employed 1.75 mm diameter of PLA filament as its primary material. After completing all layers development, the HSWR became ready for experiments (Figure 1(b)).

The major components of the investigated rotor comprise two blades mounted over a shaft without gap distance using lower and upper end plates. The rotor design parameters were selected with regard to the literature researches and the potential of the used 3D printing machine. The overall geometrical parameters are depicted in Table 1.

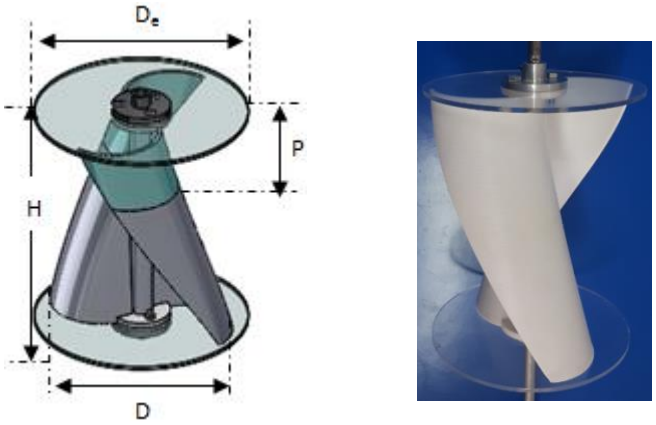

(a) (b)

Fig. 1. HSWR (a) Digital model (b) 3D printed model

Table 1
Geometrical parameters of the studied HSWR

Parameter	Value
Rotor diameter, D	160 mm
Rotor height, H	200 mm
End plate diameter, D_e	165 mm
End plate thickness	4 mm
Shaft diameter, s	10 mm
Number of Blades	2
Blade chord, d	80 mm
Blade thickness	2 mm
Blade twist angle, ψ	90°
Overlap distance, e	0 mm
Blade portion, P	48.5 mm

2.2 Wind Tunnel

The wind tunnel illustrated in Figure 2 was used to conduct experimental tests to recognize the investigated rotor aerodynamic features. It mainly consists of a drive section, a collector, a test section, a diffuser and a settling chamber used to make the airflow straight. The shape of the test section, in which the HSWR is placed, is a parallelepiped with a width of 0.4 m and equal height and a length of 0.8 m where wind velocity ranges between 0 and 9 $m.s^{-1}$. The air speed is controlled by varying the frequency of the ventilation fan of the vacuum cleaner mounted in the settling chamber. A hot wire anemometer AM-4204 was used to measure the air velocity.

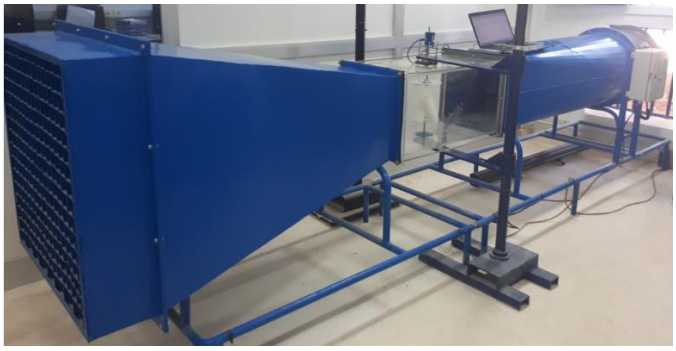

Fig. 2. Wind tunnel

2.3 Experimental Approach

The present experimental study is concerned with HSWR. It was to put the proposed rotor in the middle of the test section. Two ball bearings were fixed on either side to ensure the axis rotational guidance and to support the rotor. At a chosen velocity (U_∞) equal to U_∞=9 m.s^{-1} corresponding to a Reynolds number (R_e) equal to R_e= 9.8×10^4, the incoming wind force generates the blade rotation and then a rotating power is getting as a result. A static and a dynamic approach were planned.

For the static approach, and relative to the wind direction, for each angular position ranging from 0° to 360° in a step of 10°, the HSWR was blocked and the static torque T_s was evaluated with the use of a static digital TQ-8800 torque meter as shown in Figure 3.

1) Static torque meter sensor
2) Static torque meter digital display
3) Gradual disk

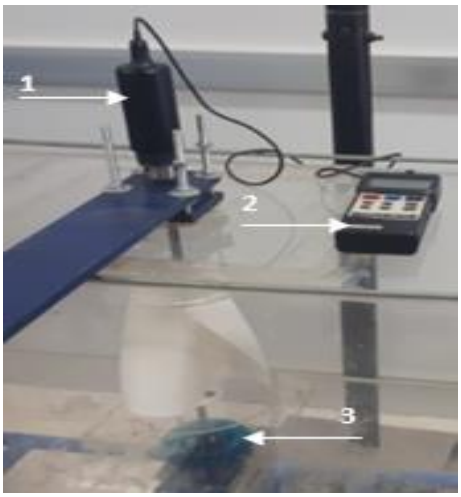

Fig. 3. Static approach instruments

For the dynamic approach, for a fixed air velocity equal to U_∞=9 m.s^{-1} relating to R_e=9.8×10^4 Reynolds number, the rotation of the examined HSWR was braked with the application of loads. In this respect, the rotor was gradually loaded and the rotor rotational speed (Ω) as well as the dynamic torque (T) were recorded for each load. Ω was estimated with the use of a CA-27 digital tachometer model and T was computed through the use of a dynamic torque meter in digital format. Indeed, the corresponding instantaneous torque was exhibited on the computer interface through the installed software EMPEROR. The needed experimental apparatus are portrayed in Figure 4.

1) Dynamic torque meter sensor
2) Digital Torque meter display
3) Digital Torque meter display
4) Tachometer

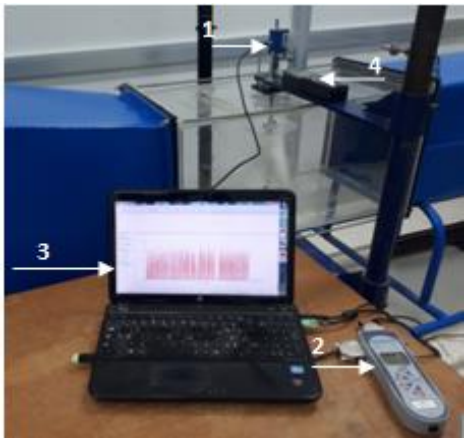

Fig. 4. Dynamic approach instruments

3. Numerical Method

The Computational Fluid dynamics (CFD) have been invested to settle the fluid flow issues in multiple applications for years [17-23]. In the current study, three-dimensional transient simulations were performed applying the ANSYS FLUENT 17.0. The wind flow modelling around the examined rotor relies on resolving the Navier-Stokes equations that regulate it [24-26].

3.1 Computational Domain and Boundary Conditions

Resting upon ANSYS Design Modeler, the computational domain was generated and the necessary boundary conditions were identified as recorded in Figure 5. The computational domain branched out into two sub-domains. A steady one stood for the test vein. A rotating one stood for the cylindrical domain characterized by a rotating domain diameter (D_r) equal to D_r= 1.1D. This last contained the investigated HSWR. An interface was set to border both domains. Concerning the boundary conditions, a velocity of U_∞= 9 m.s^{-1} was defined as an inlet upstream. Downstream, an atmospheric pressure was defined as an outlet.

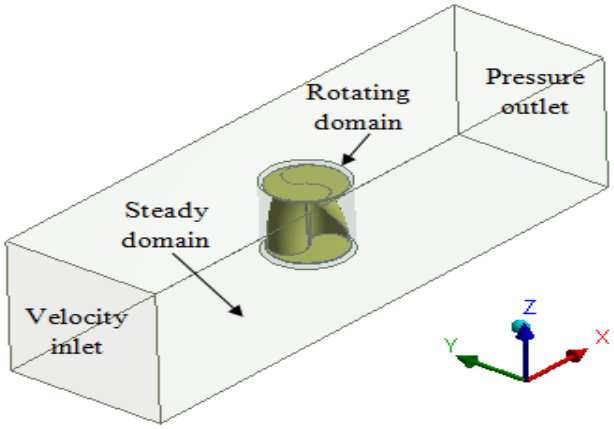

Fig. 5. Computational domain and boundary conditions

To choose the convenient diameter of the rotating domain, a rotating domain size effect study was investigated. Indeed, four domains as shown in Figure 6 with a cylindrical form and characterized by diameter sizes equal to D_r=1.1 D, D_r=1.4 D, D_r=1.8 D and D_r=2.2 D were putted in test. The choice of the suitable diameter is based on the comparison between the numerical findings related to each one of them with the elaborated experimental results.

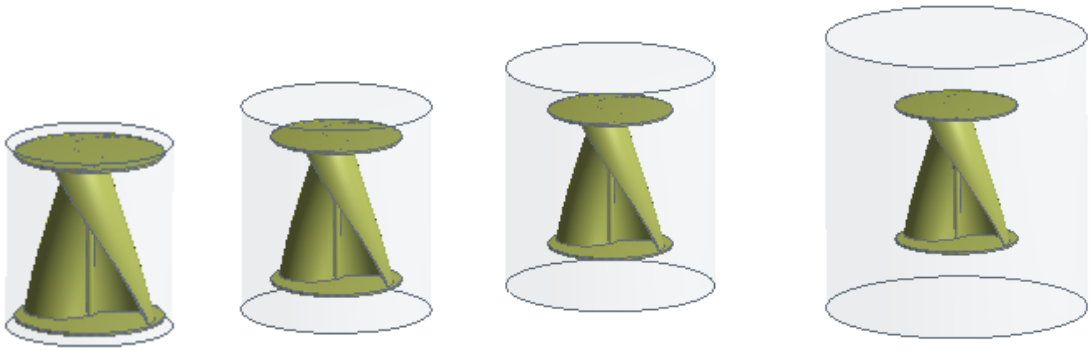

(a) (b) (c) (d)

Fig. 6. Rotating domains putted in test (a) D_r=1.1 D (b) D_r=1.4 D (c) D_r=1.8 D (d) D_r=2.2 D

3.2 Grid Generation

The computational domain is imported to the ANSYS meshing interface. Due to the complex geometry of the HSWR, an unstructured mesh with tetrahedral elements was used for the overall domain. Indeed, a mesh refinement was realized wherein the size of the generated mesh was progressively increased until the computational results didn't undergo a significant alteration. The simulations were realized with four grid sizes named coarse, medium, fine and extra fine having 260,000, 570,000, 880,000 and 1.3 million nodes, respectively. Figure 7 evinces the four generated grids. Finer mesh was created in the rotating zone compared to the steady region. To capture the rapid variations of the aerodynamic characteristics around the HSWR, it was recommended to create fine mesh near the rotor walls sufficiently: boundary layer mesh. Thus, 20 prismatic layers were created at the level of boundary layers and especially at the rotor blades.

The suitability of the generated mesh depends on the choice of the distance of the first mesh node from the rotor walls (y_n). y^+ is the appropriate parameter to estimate y_n based on Eq. (1). The accurate value of y^+ depends on the turbulence model walls law. As the SST k-ω model was used under this study, an y^+ almost equal to 1 was associated. Twenty prismatic layers with 1.2 growth rate were generated.

$$y^+ = \frac{\rho u_t y_n}{\mu} \tag{1}$$

Where ρ is the air density (kg.m^{-3}), u_t is the friction velocity (m.s^{-1}) and μ is the viscosity of the fluid (Pa.s).

A grid sensitivity study was done so that the generated chosen mesh gives a good prediction and an agreement with the elaborated experimental results.

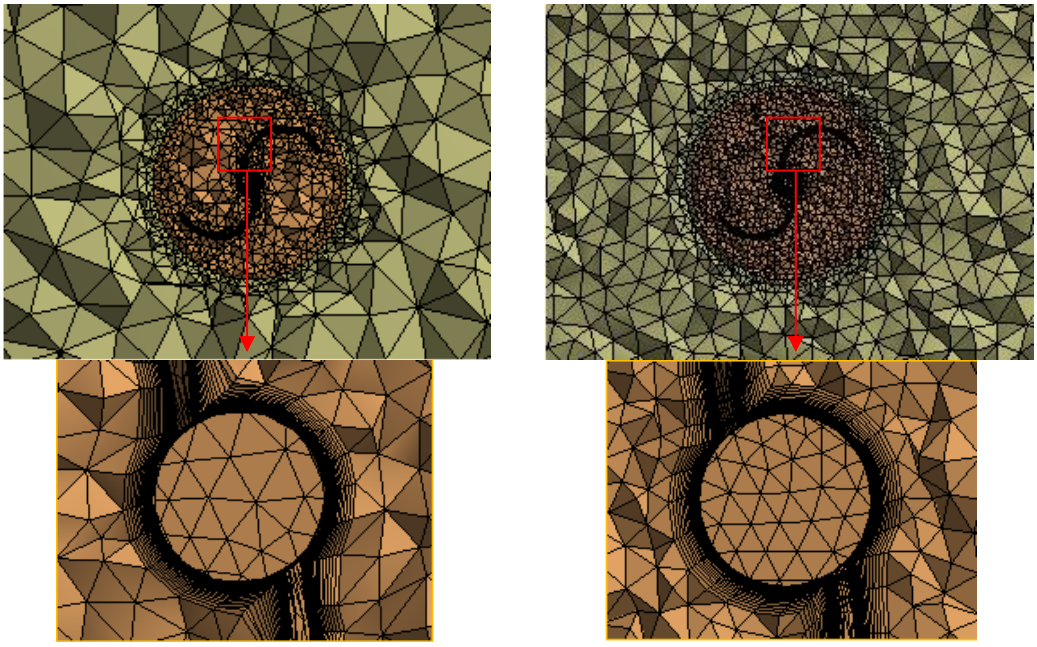

(a) (b)

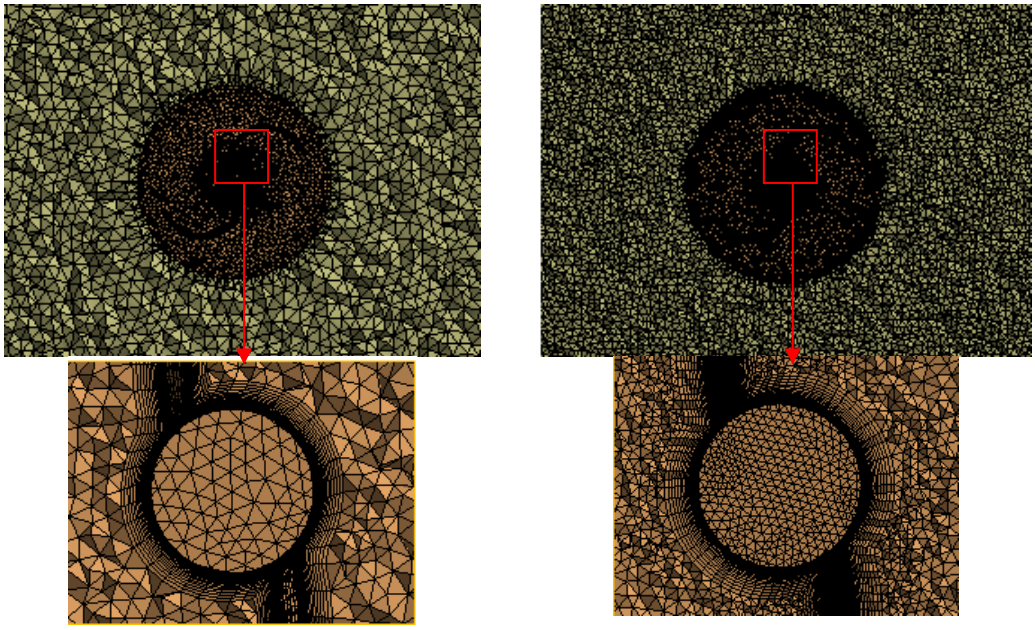

(c) (d)

Fig. 7. Generated grids (a) Coarse (b) Medium (c) Fine (d) Extra fine

3.3 Turbulence Model and Solver Settings

The flow surrounding the HSWR is naturally turbulent. For these criteria, transient simulations were carried out. A suitable time step (Δt) was chosen following Eq. (2).

$$\Delta t = \frac{\Delta \theta}{\Omega} \tag{2}$$

Where θ the HSWR is shaft angular position (rad) and Ω is the HSWR rotational speed (rad s^{-1}).

The time step chosen in this study corresponded to 1° rotation of the HSWR. 50 was the number of iterations taken per time step so that the wind flow was readjusted and renewed until being stabilized. Calculations were done for six complete rotor revolutions. The consistent state of the flow was obtained after four revolutions. The details were so saved from the fourth cycle. To reach the convergence, the values of the obtained results for each iteration should be closer to the previous one. In fact, relaxation factors are necessary to amortize the solution from the previous one so that the stability is reached. They were set equal to 0.3 for the pressure, 0.8 for the momentum, the turbulent kinetic energy and the turbulent dissipation rate, and 1 for the turbulent viscosity and the body force. The momentum, turbulence and continuity residuals values were settled equal to 10^{-5} to monitor the convergence.

The resolution of the fluid dynamics problems is based on the Reynolds-Averaged Navier-Stokes equations. Finite Volume Method was used to discretize them. The convective terms as well as the temporal ones were discretized using the Second order Up-wind scheme. The SIMPLE scheme (Semi-Implicit Methods for Pressure-Linked Equation) was used to infer the relation between the pressure and the velocity in the overall domain.

The Navier-Stokes governing equations according to a Newtonian fluid are prescribed under two equations: the continuity expressed in Eq. (3) and the momentum expressed in Eq. (4).

$$\frac{\partial \rho}{\partial t}+\frac{\partial\left(\rho u_i\right)}{\partial x_i}=0 \tag{3}$$

Where t is the time (s) and u_i is the velocity component defined in the x_i coordinate direction x_i=(x,y,z).

$$\frac{\partial\left(\rho u_i\right)}{\partial t}+\frac{\partial\left(\rho u_i u_j\right)}{\partial x_j}=-\frac{\partial p}{\partial x_i}+\frac{\partial}{\partial x_j}\left[\mu\left(\frac{\partial u_j}{\partial x_j}+\frac{\partial u_j}{\partial x_i}-\frac{2}{3}\delta_{ij}\frac{\partial u_i}{\partial x_i}\right)\right]+\frac{\partial\left(-\rho\overline{u_i' u_j'}\right)}{\partial x_j}+F_i \tag{4}$$

Where p is the pressure (Pa) and F_i is the external forces applied (N).

The components of the Reynolds stress tensor are expressed mathematically through Eq. (5).

$$-\rho\overline{u_i' u_j'}=\mu_t\left(\frac{\partial u_i}{\partial x_j}+\frac{\partial u_j}{\partial x_i}\right)-\frac{2}{3}\rho k\delta_{ij} \tag{5}$$

Where μ_t is the turbulent viscosity (Pa.s), x_i, x_j are the Cartesian coordinate, k is the turbulent kinetic energy (Pa.s) and δ_{ij} is the Chronecker indices.

Four turbulence models the Standard k-ε, the RNG k-ε, the Realizable k-ε and the SST k-ω were putted to test under this study to show the effect of the turbulence model on aerodynamic and performance characteristics of the HSWR and then to select the one that gives a good accordance with experimental results.

The Shear Stress Transport SST k-ω model was selected for the current simulations. Many researchers have demonstrated its good capability to modelize the wind turbines and its good ability to predict the flow patterns [27-30]. In fact, the SST k-ω model combines the accuracy and the robustness of the k-ω model in the near wall regions with the free flow of the k-ε model in the far wall regions.

The turbulence kinetic energy (k) is expressed as follows:

$$\frac{\partial(\rho k)}{\partial t}+\frac{\partial\left(\rho u_i k\right)}{\partial x_i}=\frac{\partial}{\partial x_i}\left[\left(\mu+\frac{\mu_t}{\sigma_k}\right)\mathrm{grad}(k)\right]+2\mu_t\frac{\partial u_i}{\partial x_j}\cdot\frac{\partial u_i}{\partial x_j}-\frac{2}{3}\rho k\frac{\partial u_i}{\partial x_j}\delta_{ijk}-\beta^*\rho k\omega \tag{6}$$

The specific dissipation rate (ω) is written as follows:

$$\begin{aligned}&\frac{\partial\rho\omega}{\partial t}+\frac{\partial\left(\rho u_i\omega\right)}{\partial x_i}=\\&\frac{\partial}{\partial x_i}\left[\left(\mu+\frac{\mu_t}{\sigma_{\omega,1}}\right)\mathrm{grad}(\omega)\right]+\gamma_2\left(2\rho\frac{\partial u_i}{\partial x_j}\cdot\frac{\partial u_i}{\partial x_j}-\frac{2}{3}\rho\omega\frac{\partial u_i}{\partial x_j}\delta_{ij}\right)-\beta_2\rho\omega^2+2\frac{\rho}{\sigma_{\omega,2}\omega}\frac{\partial k}{\partial x_k}\frac{\partial\omega}{\partial x_k}\end{aligned} \tag{7}$$

Where μ is the dynamic viscosity (Pa.s) and β^*, β_2, σ_k, $\sigma_{\omega,1}$, $\sigma_{\omega,2}$ and γ_2 are the constants of the SST k-ω turbulence model.

4. Experimental Results

The performance traits of the wind turbines are determined by the static torque coefficient (C_{Ts}) as a function of the angular position (Θ) and the dynamic torque coefficient (C_T) and the power coefficient (C_p) as a function of the tip speed ratio (λ).

Using Eq. (8), the static torque coefficient is calculated. It reflects the self-starting criteria of the HSWR.

$$C_{Ts} = \frac{T_s}{\frac{1}{2}\rho R A U^2_{\infty}} \tag{8}$$

Where T_s is the static torque (N), ρ is the air density (kg.m^{-3}), R is the HSWR radius (m), U_∞ is the incoming wind velocity (m.s^{-1}) and A is the projected area calculated as follows:

$$A = DH \tag{9}$$

Where D and H are the diameter and the height of the rotor (m), respectively.

The tip speed ratio, the torque coefficient and the power coefficient are calculated based on Eq. (10), Eq. (11) and Eq. (12), respectively.

$$\lambda = \frac{R\Omega}{U_{\infty}} \tag{10}$$

$$C_T = \frac{T}{\frac{1}{2}\rho R A U^2_{\infty}} \tag{11}$$

$$C_p = C_T \lambda \tag{12}$$

Where R stands for the HSWR radius (m), Ω expresses the rotor rotational speed (rad.s^{-1}), T represents the dynamic torque (N).

The static torque is often used to describe the starting feature of the HSWR. Figure 8 shows the C_{Ts} versus the angular position for the tested rotor. As it is clear, the variation of the static torque coefficient is periodic having a 180° cycle. The static torque coefficient increases gradually until reaching its peak. The highest C_{Ts} take the value of 0.161 for Θ=100°. For the rest of the cycle, the static torque coefficient decreases to attain its minimum at Θ=180°. The maximum value of C_{Ts} is derived from a maximum quantity of the air that attacked the concave side of the HSWR blade at the corresponding angular position. However, its minimum value is inferred from the force of the air which did not properly move to the concave side of the blade at the corresponding angular position. As the graph only indicates positive and important values of C_{Ts}, then the studied HSWR highlights a good starting ability.

The experimental power and torque coefficients for the studied HSWR are highlighted respectively in Figure 9(a) and Figure 9(b). Departing from Figure 9(a), the highest value of the power coefficient ($C_{p,max}$=0.1224) is recorded at λ=0.69. Above it, Cp drops. In terms of the torque coefficient, its maximum value ($C_{T,max}$=0.214) is found at λ=0.42. Referring to this value, C_T decays

even with the increment of λ. In this regard, the more loads are applied, the more the rotation of the helical rotor is inhibited and the more the produced torque rises.

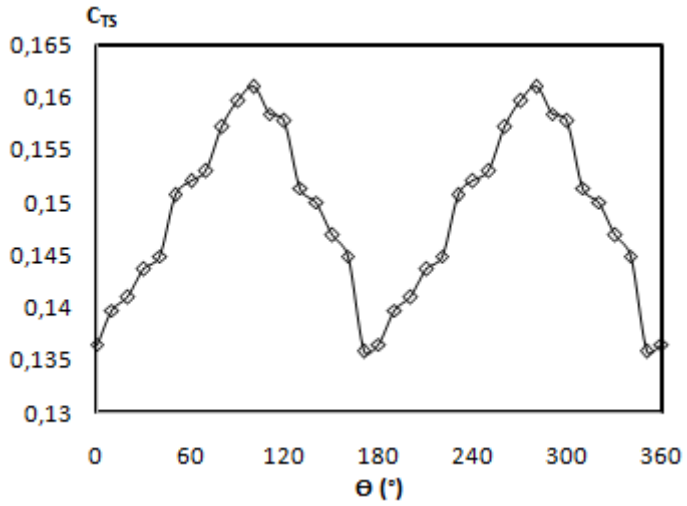

Fig. 8. Static torque coefficient versus azimuth

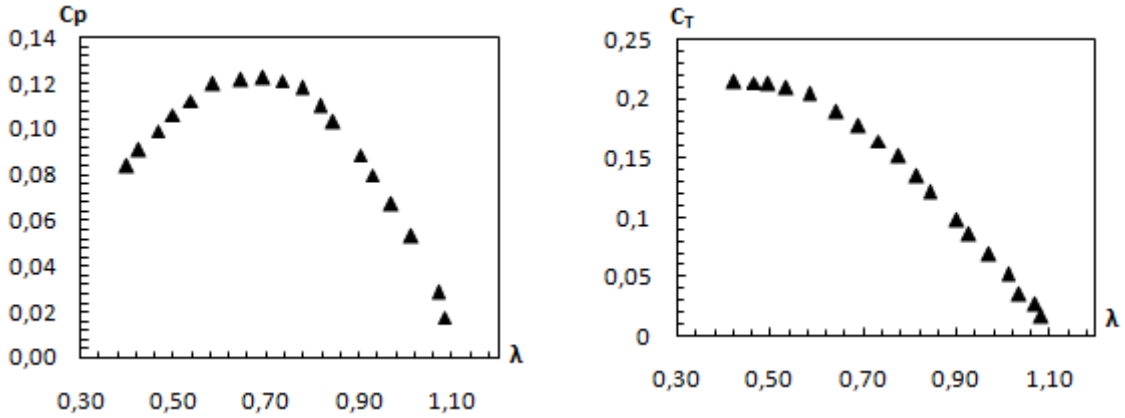

(a) (b)

Fig. 9. Performance characteristics (a) Power coefficient (b) Torque coefficient

5. Numerical Model Choice and Validation

5.1 Rotating Domain Size Effect

The torque coefficient of the HSWR in the last revolution was chosen as an output parameter to show the effect of the rotating domain size. Figure 10(a) depicts the effect of the rotating domain diameter D_r on the torque coefficient at λ=0.73. From these results, it is clear that the choice of the rotating domain influences the evolution of the torque coefficient. In fact, its averaged value increases with the increase of D_r and subsequently the error is increased. Figure 10(b) evinces a comparison, in a range of tip speed ratio varying from 0.4 to 1.2, between the elaborated experimental power coefficients and the numerical ones for the tested rotating domains. From these findings, the increase of the rotating domain size is accompanied with an increase in the rotor power coefficient. A good agreement between the experimental power coefficient and the numerical one relative to D_r=1.1 D was found. In these conditions, the error is arround 5%. However, the error becomes more importatnt while increasing the rotating domain. Its maximum value is recorded for D_r=2.2 D. Thus, the rotating domain with D_r=1.1 D is the choosen one.

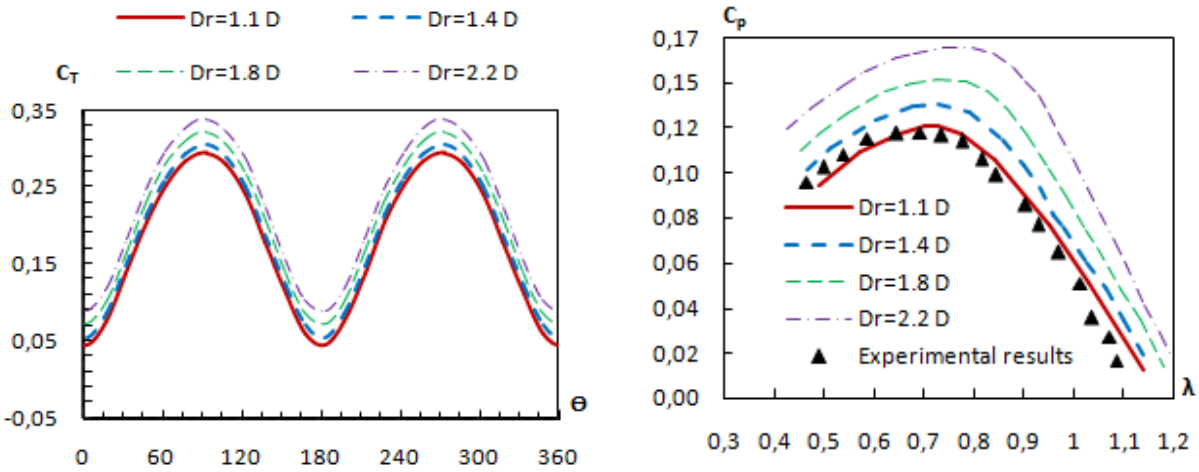

Fig. 10. Effect of the rotating domain size on the HSWR performance (a) Torque coefficient (b) Power coefficient

5.2 Grid Sensitivity Effect

As for the grid sensitivity study, for a fixed rotating domain equal to D_r=1.1 D, four grid sizes called extra fine, fine, medium and coarse having 1.3 million, 880,000, 570,000 and 260,000 nodes, respectively, were assessed. Figure 11(a) foregrounds, at λ=0.73, the influence of the grid sensitivity on the torque coefficient. The torque coefficient relative to the coarse and the medium grids are out of step in comparison with those of the fine and the extra fine, which appears to be close to each other. The coarse and the medium grids are so dismissed. Figure 11(b) enacts a comparison between experimental and numerical power coefficients for the tested grids for an interval of λ varying from 0.4 to 1.2. The fine and the extra fine grids go in good accordance with the experimental results. The error compared to the experimental power coefficient is more remarkable for the coarse and the medium grids. The more the nodes number increase the more the error decreases and the numerical predicted results get closer to experimental ones. As a matter of fact, in order to spare time calculation, the fine mesh was selected with an average error of 5% in comparison with experimental findings.

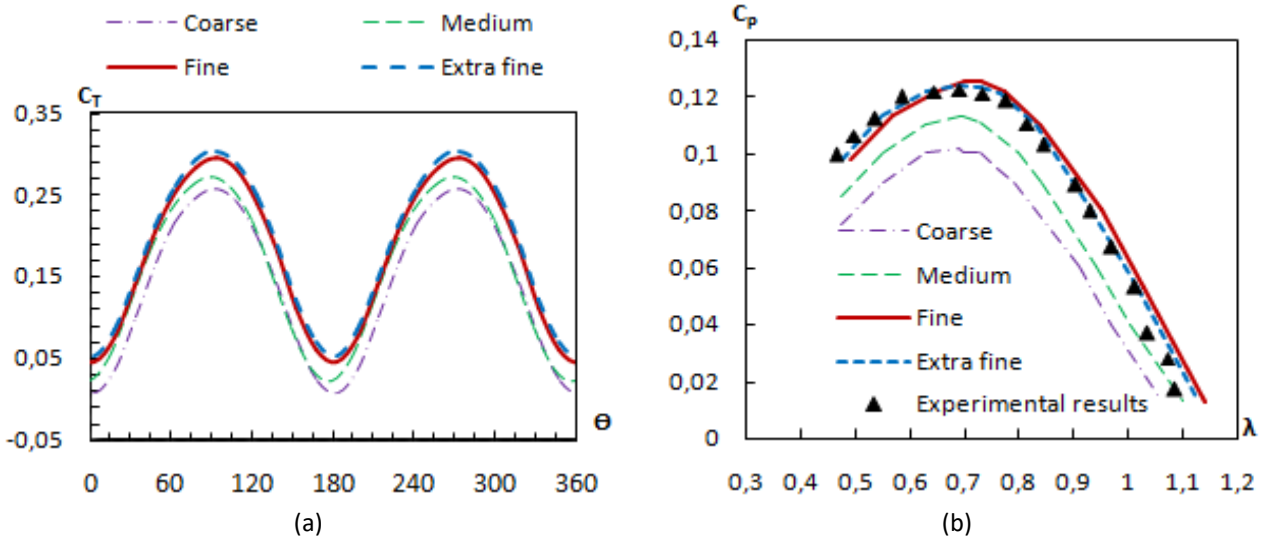

Fig. 11. Effect of the generated grid on the HSWR performance (a) Torque coefficient (b) Power coefficient

5.3 Turbulence Model Effect

With regard to the turbulence model study, for a fixed rotating domain equal to D_r=1.1 D, four turbulence models namely the Standard k-ε, the RNG k-ε, the Realizable k-ε and the SST k-ω were assessed. Findings are outlined in Figure 12. According to Figure 12(a), it is obvious that the torque coefficient relative to the SST k-ω and the Realizable k-ε turbulence models are extremely close. Yet, the RNG k-ε and the standard k-ε are far away from them. Figure 12(b) evinces a comparison between experimental and numerical power coefficients for the tested turbulence models for an interval of λ varying from 0.4 to 1.2. A good consistency between the experimental power coefficient and the numerical ones is inferred from the SST k-ω and the Realizable k-ε models. The gap seems more significant for the standard k-ε and the RNG k-ε. Resting on those results, and since the SST k-ω has been the most convenient model for multiple scientists in aerodynamic areas, it was chosen with an average error of 5% compared to the experimental results.

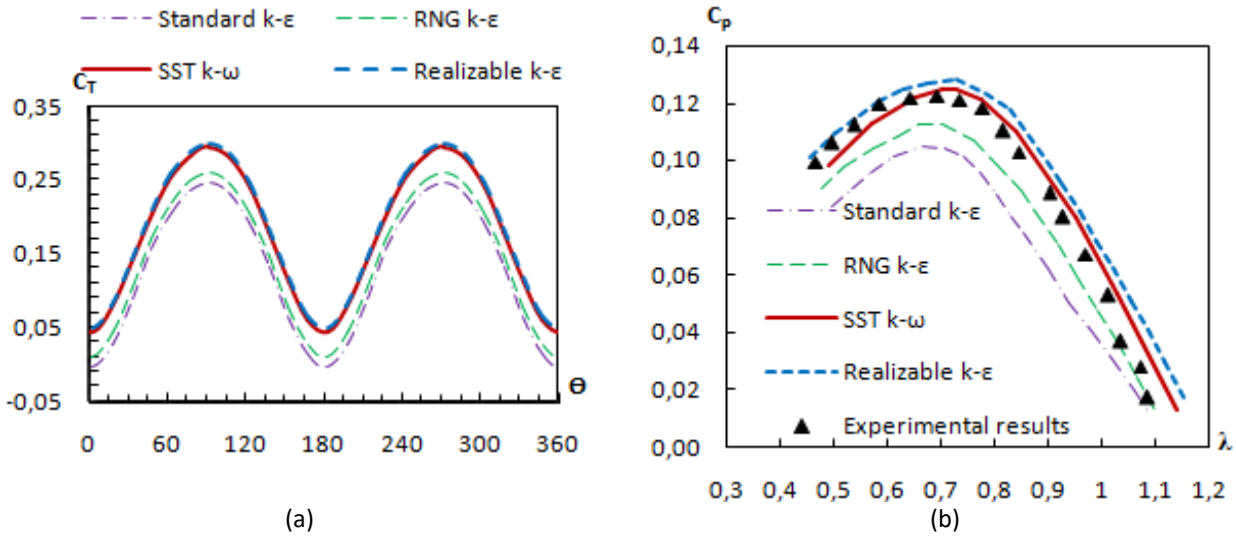

(a) (b)

Fig. 12. Effect of the turbulence model on the HSWR performance (a) Torque coefficient (b) Power coefficient

5.4 Numerical Model Validation and Aerodynamic Characteristics

5.4.1 Numerical model validation

The superposition of the experimental and the numerical power coefficients for the HSWR are summarized in Figure 13. It is clear that the adopt numerical model with the selected parameters investigated above proved to be in line with the elaborated experimental findings with an average error equal to 5%. Next, the numerical model was validated and became relevant for examining the HSWR performance betterment.

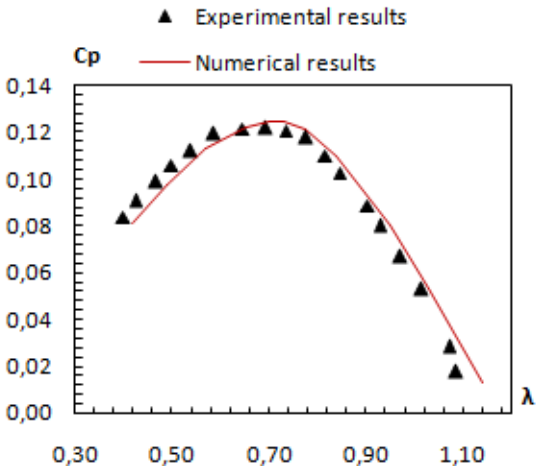

Fig. 13. Validation of the numerical model

5.4.2 Aerodynamic characteristics

Figure 14 displays, at λ=0.73, the distribution of the investigated HSWR magnitude velocity in the longitudinal planes defined, respectively, by z=0.097 m and y=0 m. It is quite clear that it is uniform upstream the HSWR with a value of U=9 m.s^{-1} as defined in the inlet boundary condition. Around the rotor, it goes down. A stagnating point lies on the returning blade convex side. In fact, the rotor acts as an obstacle in front of the incoming wind flow which leads to a deceleration in the surrounding area. The maximum velocity region lies on the advancing blade attack point. It achieves U=21.57 m.s^{-1}. This fact is associated with the lift force produced there which is responsible of the HSWR rotation. The velocity distribution highlights also the appearance of vortices on the concave side of both advancing and returning blades. It relies with the air flow passage from one blade to the other while the rotor rotates. A deceleration zone is recorded downstream the rotor, which is deflected up referring to the centrifugal force created with the rotor rotation. Getting far from the rotor, the velocity goes down and then rises gradually. As a result, a wake phenomenon is introduced.

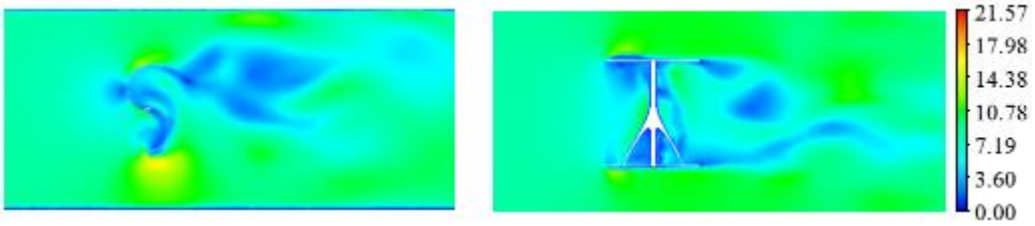

(a) (b)

Fig. 14. Magnitude velocity (m.s^{-1}) distribution (a) z=0.097 m (b) y=0 m

Figure 15 presents the total pressure distribution in the longitudinal planes defined, respectively, by z=0.097 m and y=0 m at λ=0.73. Upstream, a high pressure zone is highlighted as the velocity there was weak. It is clear also that, the highest pressure zone (p=118.57 Pa) is found on the convex side of the returning blade. It is related to the drag force created there. Moreover, the lowest pressure zone is found on the concave side of the advancing blade (p=53 Pa). As a result, the returning and the advancing blades of the HSWR display different pressure distribution. The difference in terms of pressure is what causes the rotor to rotate anti-clockwise. Downstream, low pressure zone with a value around p=20 Pa is evinced. It is related to wake phenomenon as the velocity there starts to increase gradually.

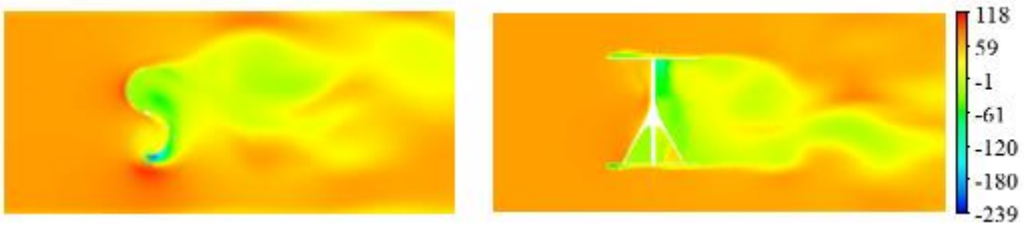

(a) (b)

Fig. 15. Total pressure (Pa) distribution (a) z=0.097 m (b) y=0 m

Figure 16 plots the distribution of the turbulent kinetic energy (k) in the longitudinal planes defined, respectively, by z=0.097 m and y=0 m at λ=0.73. The turbulent kinetic energy, upstream the rotor, is nearly negligible as the velocity there is very weak. It rises slightly around the HSWR and exhibits a higher-value zone at the advancing and the returning blade attack points. As a matter of fact, more wind energy is produced there derived from higher-value of velocity caused by the lift force generation. Downstream the rotor, a considerable rise is detected associated with the wake phenomenon stated previously. Maximum turbulent kinetic energy value proves to be equal to k= 7.71 J.kg^{-1}.

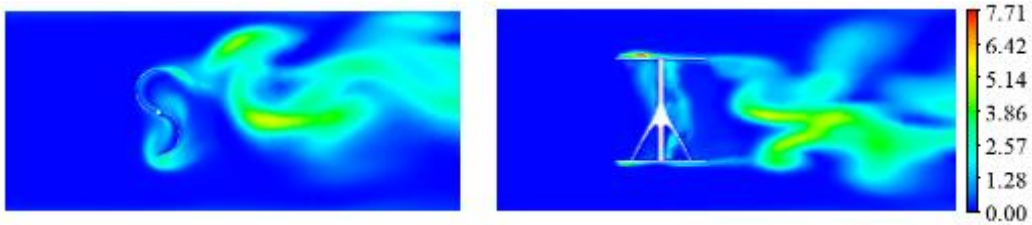

(a) (b)

Fig. 16. Turbulent kinetic energy (J.kg^{-1}) distribution (a) z=0.097 m (b) y=0 m

Figure 17 shows the distribution of the turbulent viscosity around the HSWR in the longitudinal planes defined, respectively, by z=0.097 m and y=0 m at λ=0.73. It is obvious that the turbulent viscosity is very low upstream the rotor. It becomes slightly remarkable at the rotating domain. The turbulent viscosity increases around the rotating domain and shows more zones in front of the concave side of both the advancing and the returning blades. Downstream away from the rotor, zones highlighting maximum value of the turbulent viscosity became more and more remarkable. The more the flow is turbulent the more eddies appear. In fact the turbulent flow can be considered as an irregular eddy. The air velocity at each point of the computational domain is occurring continuously changes in direction and magnitude due to the fluctuations. Getting away from the rotor, there is a flow wake creation.

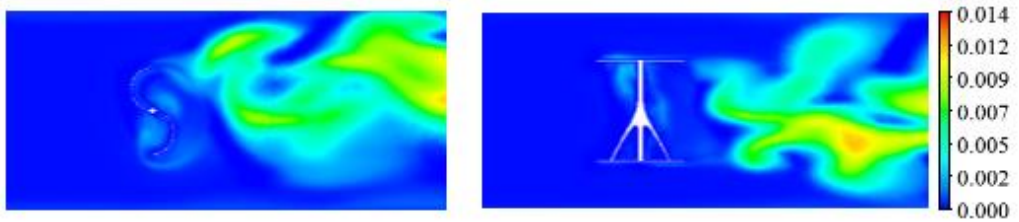

(a) (b)

Fig. 17. Turbulent viscosity (Pa.s) distribution (a) z=0.097 m (b) y=0 m

Figure 18 shows the turbulent intensity distribution for the HSWR in the longitudinal planes defined, respectively, by z=0.097 m and y=0 m at λ=0.73. Upstream, the turbulent intensity seems to

be weak. Approaching to the rotating domain, it is noticed that the turbulent intensity increases and shows more zones in front of the concave side of both the advancing and the returning blades. Downstream, a remarkable high turbulent intensity zone appears with a symmetrical aspect (Figure 18(b)). In fact, the flow becomes more turbulent due to more vortices formation there which causes more detected viscosity resulting in a deficit in the velocity values introducing so the wake of the flow downstream.

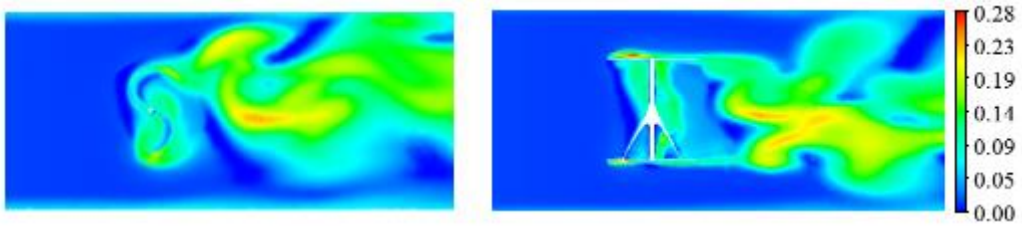

(a) (b)

Fig. 18. Turbulent intensity distribution (a) z=0.097 m (b) y=0 m

6. Conclusion

Under this study, experimental and numerical tests were performed to assess the efficiency as well as the feasibility of a HSWR. The investigated rotor was created relying upon 3D printing machine. Experimental tests were conducted in wind tunnel having a test section market with a uniform air flow velocity of U_∞=9 m.s^{-1}. The maximum experimental power coefficient $C_{p,max}$=0.1224 was recorded at λ=0.69. The numerical study was run using Ansys Fluent 17.0 software. Grid, turbulence model and rotating domain size tests were undertaken.

It was proven that the grid structure and size, the turbulence model as well as the size of the rotating domain have an effect on the computational findings. With regard to the grid choice, the selected one was chosen to have an important number of cells with good accuracy and time saving. For the turbulence model, the SST k-ω was selected with respect to the previous works provided in the literature and for the good agreement shown with the elaborated experimental results. Finally, the selected rotating domain was chosen as it gave good agreement and improves the numerical findings compared to the others. Under these conditions, the numerical model with the selected parameters was found in agreement with the elaborated experimental findings with an average error equal to 5%. The maximum numerical power coefficient $C_{p,max}$=0.124 at λ=0.73.

The undertaken research work could provide with deeper insights into the aerodynamic features of the air flow of a helical Savonius wind rotor for the benefit of both engineers and designers with the objective of promoting its performance.

Acknowledgements

This research was not funded by any grant. The authors are thankful to the Laboratory of Electro Mechanic Systems (LASEM) members for the valuable financial assistance.

References

[1] Roslan, Siti Amni Husna, Zainudin A. Rasid, and Ahmad Kamal Ariffin. "Extended blade element momentum theory for the design of small-scale wind turbines." *Journal of Advanced Research in Applied Mechanics* 101, no. 1 (2023): 62-75. https://doi.org/10.37934/aram.101.1.6275.

[2] Kamdar, Ismail, and Juntakan Taweekun. "A Comparative Study of Wind Characteristics Between South-Western and South-Eastern Thailand Using Different Wind Turbine Models." *Journal of Advanced Research in Fluid Mechanics and Thermal Sciences* 92, no. 1 (2022): 149-161. https://doi.org/10.37934/arfmts.92.1.149161.

[3] Alotaibi, Alowaid, Mohd Khairul Hafiz Muda, Faizal Mustapha, Izhal Abdul Halin, and Noorfaizal Yidris. "Perpetual Motion Wind Turbine Generator for Novelty Energy Harvesting System; Conceptual Design Approach." *Journal of Advanced Research in Fluid Mechanics and Thermal Sciences* 94, no. 2 (2022): 166-173. https://doi.org/10.37934/arfmts.94.2.166173.

[4] Akwa, João Vicente, Gilmar Alves da Silva Júnior, and Adriane Prisco Petry. "Discussion on the verification of the overlap ratio influence on performance coefficients of a Savonius wind rotor using computational fluid dynamics." *Renewable energy* 38, no. 1 (2012): 141-149. https://doi.org/10.1016/j.renene.2011.07.013

[5] Roy, Sukanta, and Ujjwal K. Saha. "Investigations on the effect of aspect ratio into the performance of Savonius rotors." In *Gas turbine India conference*, vol. 35161, p. V001T07A002. American Society of Mechanical Engineers, 2013. https://doi.org/10.1115/GTINDIA2013-3729

[6] Zhao, Zhenzhou, Yuan Zheng, Xiaoyun Xu, Wenming Liu, and Guoxiang Hu. "Research on the improvement of the performance of Savonius rotor based on numerical study." In *2009 International Conference on Sustainable Power Generation and Supply*, pp. 1-6. IEEE, 2009.

[7] Jeon, Keum Soo, Jun Ik Jeong, Jae-Kyung Pan, and Ki-Wahn Ryu. "Effects of end plates with various shapes and sizes on helical Savonius wind turbines." *Renewable energy* 79 (2015): 167-176. https://doi.org/10.1016/j.renene.2014.11.035

[8] Zheng, M., X. Zhang, L. Zhang, H. Teng, J. Hu, and M. Hu. "Uniform test method optimum design for drag-type modified Savonius VAWTs by CFD numerical simulation." *Arabian Journal for Science and Engineering* 43 (2018): 4453-4461. https://doi.org/10.1007/s13369-017-2920-5

[9] Kothe, Leonardo Brito, Sérgio Viçosa Möller, and Adriane Prisco Petry. "Numerical and experimental study of a helical Savonius wind turbine and a comparison with a two-stage Savonius turbine." *Renewable Energy* 148 (2020): 627-638. https://doi.org/10.5380/reterm.v18i2.70794

[10] Lee, Jae-Hoon, Young-Tae Lee, and Hee-Chang Lim. "Effect of twist angle on the performance of Savonius wind turbine." *Renewable Energy* 89 (2016): 231-244. https://doi.org/10.1016/j.renene.2015.12.012

[11] Alom, Nur, and Ujjwal K. Saha. "Influence of blade profiles on Savonius rotor performance: Numerical simulation and experimental validation." *Energy Conversion and Management* 186 (2019): 267-277. https://doi.org/10.1016/j.enconman.2019.02.058

[12] Tian, Wenlong, Zhaoyong Mao, Baoshou Zhang, and Yanjun Li. "Shape optimization of a Savonius wind rotor with different convex and concave sides." *Renewable energy* 117 (2018): 287-299. https://doi.org/10.1016/j.renene.2017.10.067

[13] Nurmutia, Syahreen, Bukhari Manshoor, Amir Khalid, Izzuddin Zaman, Djamal Hissein Didane, Reazul Haq Abdul Haq, Mohammad Fahmi Abdul Ghafir *et al.,* "Performance Analysis on a New Design of Blade Shape for Savonius Wind Turbine." *Journal of Advanced Research in Fluid Mechanics and Thermal Sciences* 108, no. 1 (2023): 173-183. https://doi.org/10.37934/arfmts.108.1.173183.

[14] Abdelsattar, Sohib, Nurul Asyikin Abu Bakar, and Noorfazreena Mohammad Kamaruddin. "Performance of Savonius Turbines with Tubercles Inspired by Humpback Whales." *Journal of Advanced Research in Applied Sciences and Engineering Technology* 31, no. 1 (2023): 68-78. https://doi.org/10.37934/araset.31.1.6878.

[15] Mohamed, M. H., G. Janiga, E. Pap, and D. Thévenin. "Optimization of Savonius turbines using an obstacle shielding the returning blade." *Renewable Energy* 35, no. 11 (2010): 2618-2626. https://doi.org/10.1016/j.renene.2010.04.007

[16] Maldonado, R. D., E. Huerta, J. E. Corona, O. Ceh, A. I. León-Castillo, M. P. Gómez-Acosta, and E. Mendoza-Andrade. "Design, simulation and construction of a Savonius wind rotor for subsidized houses in Mexico." *Energy Procedia* 57 (2014): 691-697. https://doi.org/10.1016/j.egypro.2014.10.224

[17] Tey, Wah Yen, and Hooi Siang Kang. "Power Loss in Straight Polygon Pipe via CFD Simulation." *Progress in Energy and Environment* (2018): 1-10.

[18] Nazer, Mohamed, Muhammad Fadzrul Hafidz Rostam, Se Yong Eh Noum, Mohammad Taghi Hajibeigy, Kamyar Shameli, and Ali Tahaei. "Performance analysis of photovoltaic passive heat storage system with microencapsulated paraffin wax for thermoelectric generation." *Journal of Research in Nanoscience and Nanotechnology* 1, no. 1 (2021): 75-90. https://doi.org/10.37934/jrnn.1.1.7590.

[19] Shaharudin, Muhammad Zarif Bin, Syahar Shawal, Mazwan Mahat, and Mohd Rosdzimin Abdul Rahman. "Numerical Investigation on Thermal Performance of Various Designs Plate-Fin Heat Sinks Subject to Parallel and Impinging Flow." *Journal of Advanced Research in Numerical Heat Transfer* 13, no. 1 (2023): 66-80. https://doi.org/10.37934/arnht.13.1.6680

[20] Yanagita, Yoshiki, Kaishan Feng, Yuko Miyamura, Adi Azriff Basri, Mohammad Zuber, Siti Rohani, Abdul Aziz, Kamarul Arifin Ahmad, and Masaaki Tamagawa. "Evaluation of Virus Concentration Analysis in the Airway by CFD." *Journal of Advanced Research in Numerical Heat Transfer* 13, no. 1 (2023): 96-105. https://doi.org/10.37934/arnht.13.1.96105.

[21] Feng, Kaishan, Yoshiki Yanagita, Yuko Miyamura, Adi Azriff Basri, Mohammad Zuber, Siti Rohani, Kamarul Arifin Ahmad, and Masaaki Tamagawa. "CFD Analysis of Indoor Ventilation for Airborne Virus Infection." *Journal of Advanced Research in Numerical Heat Transfer* 14, no. 1 (2023): 1-16. https://doi.org/10.37934/arnht.14.1.116.

[22] Elfaghi, Abdulhafid MA, Alhadi A. Abosbaia, Munir FA Alkbir, and Abdoulhdi AB Omran. "CFD Simulation of Forced Convection Heat Transfer Enhancement in Pipe Using Al2O3/Water Nanofluid." *Journal of Advanced Research in Numerical Heat Transfer* 8, no. 1 (2022): 44-49.

[23] Islam, Md Saifi Bin, Muhammad Faiz Ahmed, and Abdullah Al Saad. "Numerical Investigation on the Aerodynamic Characteristics of a Wing for Various Flow and Geometrical Parameters." *Malaysian Journal on Composites Science and Manufacturing* 12, no. 1 (2023): 13-30. https://doi.org/10.37934/mjcsm.12.1.1330.

[24] Kek, Hong Yee, Huiyi Tan, Desmond Daniel Chin Vui Sheng, Yi Lee, Nur Dayana Ismail, Muhd Suhaimi Deris, Haslinda Mohamed Kamar, and Keng Yinn Wong. "A CFD assessment on ventilation strategies in mitigating healthcare-associated infection in single patient ward." *Progress in Energy and Environment* 24, no. 1 (2023): 35-45. https://doi.org/10.37934/progee.24.1.3545.

[25] Mosbahi, Mabrouk, Mouna Derbel, Mariem Lajnef, Bouzid Mosbahi, Zied Driss, Costanza Aricò, and Tullio Tucciarelli. "Performance study of twisted Darrieus hydrokinetic turbine with novel blade design." *Journal of Energy Resources Technology* 143, no. 9 (2021): 091302. https://doi.org/10.1115/1.4051483

[26] Mosbahi, Mabrouk, Mariem Lajnef, Mouna Derbel, Bouzid Mosbahi, Costanza Aricò, Marco Sinagra, and Zied Driss. "Performance improvement of a drag hydrokinetic turbine." *Water* 13, no. 3 (2021): 273. https://doi.org/10.3390/w13030273

[27] Lajnef, Mariem, Mabrouk Mosbahi, Youssef Chouaibi, and Zied Driss. "Performance improvement in a helical Savonius wind rotor." *Arabian Journal for Science and Engineering* 45, no. 11 (2020): 9305-9323. https://doi.org/10.1007/s13369-020-04770-6

[28] Jaohindy, Placide, Sean McTavish, François Garde, and Alain Bastide. "An analysis of the transient forces acting on Savonius rotors with different aspect ratios." *Renewable energy* 55 (2013): 286-295. https://doi.org/10.1016/j.renene.2012.12.045

[29] Roy, Sukanta, and Antoine Ducoin. "Unsteady analysis on the instantaneous forces and moment arms acting on a novel Savonius-style wind turbine." *Energy Conversion and Management* 121 (2016): 281-296. https://doi.org/10.1016/j.enconman.2016.05.044

[30] Nasef, M. H., Wageeh Ahmed El-Askary, A. A. Abdel-Hamid, and Hisham E. Gad. "Evaluation of Savonius rotor performance: Static and dynamic studies." *Journal of Wind Engineering and Industrial Aerodynamics* 123 (2013): 1-11. https://doi.org/10.1016/j.jweia.2013.09.009